Title: Extreme Ultraviolet Metalens by Vacuum Guiding

Authors: Marcus Ossiander[1, *, †], Maryna Leonidivna Meretska[1, †], Hana Kristin Hampel[2, †], Soon Wei Daniel Lim[1], Nico Knefz[2], Thomas Jauk[2], Federico Capasso[1, *], Martin Schultze[2, *]

Affiliations:

1 John A. Paulson School of Engineering and Applied Sciences, Harvard University; Cambridge, MA 02138, USA.

2 Institute of Experimental Physics, Graz University of Technology; 8010 Graz, Austria.

*Corresponding Authors. Email:
mossiander@g.harvard.edu, capasso@seas.harvard.edu, schultze@tugraz.at

[†] These authors contributed equally

One-Sentence Summary:

Metasurface technology can be pushed to 50 nm operating wavelengths and used to realize a metalens for extreme ultraviolet radiation.

Abstract:

Extreme ultraviolet (EUV) radiation is a key technology for material science, attosecond metrology, and lithography. Here we experimentally demonstrate metasurfaces as a superior way to focus EUV light. These devices exploit that holes in a silicon membrane have considerably larger refractive index than the surrounding material and efficiently vacuum-guide light around 50 nm wavelength. This allows the transmission phase at the nanoscale to be controlled via the hole diameter. We fabricate an EUV metalens with 10 mm focal length supporting numerical apertures of up to 0.05 and use it to focus ultrashort EUV light bursts generated via high-harmonic generation down to a 0.7 um waist. Our approach introduces the vast light-shaping possibilities provided by dielectric metasurfaces to a spectral regime lacking materials for transmissive optics.

Main Text:

Dielectric metasurfaces consist of transparent nanostructures with subwavelength separation, which manipulate the phase of light on the nanoscale (*1*). This elaborate control is revolutionizing modern optics: metasurfaces can replace bulk optics by thin and flat elements (*2*, *3*), combine multiple functions in single optical elements (*4*, *5*), and realize novel optical components inducing, e.g., freely designable optical angular momentum (*6*) and polarization (*7*, *8*). Technology, including modern semiconductor lithography, demands this design liberty for novel optical elements for ever-shorter wavelength radiation, but this development has been stalled at ultraviolet frequencies where dielectrics stop being transparent. To our knowledge, linear metaoptics have only been demonstrated down to a wavelength of ≈ 250 nm (*9–11*). Nonlinear metasurfaces reach further into the ultraviolet spectrum at the cost of indirect light-shaping mechanisms, and have currently been demonstrated down to 185 nm wavelength (*12–15*).

Inaccessible to metasurface design has been extreme ultraviolet radiation (EUV) that covers the wavelength range 10 nm – 121 nm, corresponding to 10 eV – 124 eV photon energy (*16*). This wavelength regime receives appreciable attention as a gateway to achieving attosecond temporal resolution in ultrafast spectroscopy (*17*) and lithographically fabricating nanometer scale

1   transistors in state-of-the-art semiconductor industry (*18*). However, today, all fields employing
2   EUV radiation are encumbered by handling problems arising from being limited to reflective or
3   binary optics (e.g., toroidal mirrors or Fresnel zone plates, see (*19*) for an overview of existing
4   technology). Here we present a new physical mechanism for metasurface design and demonstrate
5   how linear metasurfaces can be realized at 50 nm wavelength, thus providing the foundation for
6   general-purpose transmissive optics technology for EUV radiation.
7
8   <u>Principle of vacuum guiding and metalens design</u>
9   In the EUV, the strong absorption of most materials and their near-unity real parts of the refractive
10 index (*20*) usually prevent effective refraction or waveguiding. The refractive indexes of most
11 dielectrics in the visible spectrum are determined by electronic transitions in the ultraviolet, i.e.,
12 by resonances whose frequencies are higher than the frequency ω of visible light. In the Drude-
13 Lorentz oscillator model, this results in a complex refractive index $\tilde{n}(\omega) = n(\omega) + i\kappa(\omega)$ for
14 visible light with a real part $n \geq 1$ and a negligible absorption coefficient κ. In contrast, EUV light
15 oscillates faster than these electronic resonance frequencies, resulting in $n \leq 1$ and a large
16 absorption coefficient κ, rendering conventional transmissive metaoptics design unfeasible. For
17 the same reason, EUV manipulation must rely on reflective glancing-angle mirrors in vacuum. The
18 concept for metasurface design introduced here is visualized in Fig. 1: in the EUV spectrum,
19 vacuum/air ($n = 1$) has a refractive index that is larger than that of a pillar made from $n < 1$
20 material, therefore the pillar cannot guide or confine light. However, a void or hole ($n = 1$), i.e.,
21 the absence of material, in a layer with material index $n < 1$ can act as a waveguide core
22 surrounded by a lower index cladding. Therefore, truncated waveguide metasurfaces are possible
23 in the EUV following an inverted design scheme that tunes nanohole dimensions instead of the
24 shapes of free-standing nanostructures.
25
26 Materials with $n < 1$ to realize such metasurfaces exist throughout the EUV, e.g., aluminum,
27 silicon, and beryllium allow optics for the wavelength range from 40-90 nm, scandium and boron
28 cover 20-40 nm, and rhenium, molybdenum, and zirconium cover 10-20 nm. Fig. S1 (see (*19*))
29 compiles the refractive indexes and the transmission of these materials. Due to the availability of
30 high-brightness laser-driven tin plasma sources, 13.5 nm is a wavelength of major importance for
31 semiconductor lithography (*18*). At this wavelength, for example, ruthenium, has the complex
32 refractive index $\tilde{n} = 0.88 + 0.02i$ (*21*).
33
34 For the implementation of this concept, we choose a thin membrane of crystalline silicon as base
35 material and a cylindrical hole as polarization-independent guiding structure. These are
36 schematically shown together with the real part of the silicon refractive index in the EUV (Figs.
37 1A, C) (*22*) and the transmission through a 220 nm thick silicon layer (Fig. 1B). To highlight the
38 vacuum-guiding behavior of the holes, the simulated intensity profile of light with a vacuum
39 wavelength of $\lambda_{\text{vac}} = 50$ nm incident on such a perforated silicon membrane (80 nm hole diameter
40 in a square 120 nm x 120 nm unit cell, periodic boundary conditions, see (*19* Sec. 1) for simulation
41 details) is plotted in Fig. 1D: At the center of the membrane (110 nm after its front surface), 84 %
42 of the energy of an incident plane wave is transmitted within the hole whereas 16 % of its energy
43 is transmitted in the silicon. However, the hole only covers 34 % of the unit cell area. As most
44 power is transmitted in vacuum, absorption in silicon is limited and the overall transmission is
45 enhanced relative to that of the unstructured film: an unstructured 220 nm thick silicon membrane

transmits 28 % of incoming 50 nm light. Accounting for the 80 nm diameter hole using its area coverage would increase transmission to 52 %. Vacuum guiding increases the transmission further to 67 %.

Although perforations have been employed in nanooptics before, the presented guiding mechanism is fundamentally different from anti-guiding in holes (23), low-index guiding in air (24), or hollow-core fibers (25). Furthermore, the enhancement does not require a periodic structure, distinguishing the effect from extraordinary optical transmission (26).

To realize our EUV metasurface (Fig. 1A), with full design flexibility to emulate the phase profile of a desired optical element, we numerically create a library of metaatoms based on the transmission phase of holes with 20 nm to 80 nm diameter in a 220 nm thick silicon membrane (see (19 Sec. 1) for simulation details). Notably, between 50 nm and 62 nm wavelength, the photon energy-dependent transmission phase is widely tunable via the hole diameter and offers more than 1.5 π transmission phase coverage with an average transmission of 40 % at 50 nm (see Fig. 2A for the photon energy dependent transmission phase, Fig. 2B for the transmission and transmission phase at 50 nm, and Fig. S2 in (19) for the photon energy dependent transmission). This transmission phase coverage is enough to achieve efficient and diffraction-limited focusing, as explored, e.g., in (27). The metasurface unit cell is shown in Fig. 1C and the corresponding library is shown in Fig. 2B.

Experimental results
To experimentally prove that the vacuum-guiding concept yields viable EUV metalenses, we forward-design a focusing EUV metasurface by mimicking the wavelength-dependent transverse hyperbolic phase profile (28)

$$\varphi(r, \lambda_{\text{vac}}) = -\frac{2\pi}{\lambda_{\text{vac}}}\left(\sqrt{r^2 + f^2} - f\right) \tag{1}$$

of an aspheric lens with focal length $f = 10$ mm in vacuum at transverse position $r = \sqrt{x^2 + y^2}$ (x and y are the cartesian coordinates centered at the beam axis). This analog phase profile is matched by a simulated digital phase profile (sampled at positions x, y; $x = k\,\Delta x$; $y = l\,\Delta y$; $k, l \in \mathbb{Z}$; $\Delta x = \Delta y = 120$ nm) using the hole library (Fig. 2B), yielding a recipe for the required hole diameter distribution (Fig. 2C). The metalens is designed for a central vacuum wavelength of $\lambda_{\text{vac}} = 50$ nm where silicon features a refractive index $\tilde{n} = 0.77 + 0.02$i. The smaller than unity real part at this wavelength partially relaxes the necessity for true sub-wavelength patterning which facilitates the manufacturing of the metaoptical element. In the given implementation, the maximum feature size (80 nm) and unit cell size (120 nm) correspond to 1.2 and 1.8 times the inside-silicon-wavelength λ_{Si}, respectively. Although this does not entirely prevent the formation of low diffraction orders which contain up to 53 % of the transmitted light, it still allows the realization of numerical apertures up to NA $< \frac{\lambda_{\text{vac}}}{2\Delta x} = 0.2$ following the Nyquist theorem (29).

The demonstration sample, a free-standing metalens with a 1 mm diameter (numerical aperture NA$_{\text{max}} = 0.05$) is realized from silicon-on-insulator wafers (see (19 Sec. 2) and (19 Fig. S3) for

3

fabrication details). Figs. 2D, F show scanning-electron microscopy pictures of the final sample after metasurface etching but before membrane isolation. Fig. 2G shows a light microscopy picture of the finished membrane, with thin-film interference colors confirming the complete removal of the buried oxide layer in the lens area. We achieve the designed hole diameters (see Fig. 2D) using both diameter-dependent electron beam lithography doses and diameter-dependent fabrication offsets (see (*19* Sec. 2)). A focused-ion-beam cut (Fig. 2E) through a sample reveals holes with square sidewalls, and a partial etch of the smallest diameter holes. Due to the small transmission phase difference between a membrane with small holes and a solid membrane (see Fig. 2B), the resulting phase error is smaller than $0.1\,\pi$ and can be corrected during metaatom library calculation.

For the experimental verification of the focusing power of the metalens, we generated diverging EUV attosecond pulse trains via near-infrared femtosecond laser pulse-driven high-harmonic generation (HHG) in argon gas (*30–32*)(Fig. 3A) (*19* Sec. 3). The frequency up-conversion extends up to the 35th order (42.1 eV photon energy, 29 nm wavelength) of the driving laser pulses (1.2 eV photon energy, 1030 nm wavelength) with spectral power concentrated around the laser's odd harmonics. A toroidal EUV grating disperses the spectral components of the attosecond pulse train and creates a frequency-resolved image of the focal plane on an EUV-sensitive camera where the metasurface's effect at the design wavelength can be inspected.

Fig. 3B shows the beam profile at the focal plane of the metalens of the 21st harmonic with 25.3 eV photon energy / 49 nm wavelength (close to the design wavelength of the optics). The outline of the circular metasurface (dashed blue line) and features caused by the remaining silica aperture (dashed red/yellow lines, compare with Fig. 2G and (*19* Fig. S4)) are also visible. The bright focal spot at the metasurface center (dashed green line) presents experimental evidence for the viability of the EUV metalens to focus incident light.

Because the grazing incidence toroidal imaging grating provides a considerably smaller numerical aperture than the metasurface and introduces aberrations and astigmatism, the obtained image does not determine the focal spot diameter and underestimates the focusing power of the optical element. To determine the real focal spot size produced by the metasurface, we implement a knife-edge scan (see Fig. 3A and (*33*)) where part of the focused beam in the focal plane is gradually blocked by a razor blade translated along the x-direction indicated in Fig. 3A and the position-dependent transmitted intensity is recorded. As focusing concentrates the beam intensity along the transverse direction, the negative spatial derivative of the recorded x-dependent intensity reveals the beam profile. Figs. 3C, D display scan results for different planes along the propagation direction around the focus. Fig. 3D includes a knife-edge scan featuring a maximum negative spatial derivative, indicative of the focal plane. Under the assumption of a cylindrically symmetric Gaussian beam, the corresponding beam size is extracted by fitting an error function to the data at each position along the propagation direction (Fig. 3E) (*33*).

We observe that the metasurface focuses the illuminating beam to a minimum waist of $w_0^{\text{metasurface}} = (0.7 \pm 0.3)$ um (all reported waists w are measured using the $1/\text{e}^2$ intensity, i.e., $I\big(r = \sqrt{x^2 + y^2} = w\big) = I(r = 0)/\text{e}^2$). Using the Rayleigh-Sommerfeld diffraction integral (*34*), we calculate the minimum achievable waist $w_0^{\text{diffraction limit}} = 0.45$ um assuming diffraction-

limited focusing of our incoming beam (see Fig. S5), highlighting that the metalens already performs within 1.6 times of the diffraction limit. For further comparison, the measured propagation distance-dependent waist size $w(z)$ can be fitted to that of a focused Gaussian beam with minimum waist w_0 (*35*) in vacuum

$$w(z) = w_0 \sqrt{1 + \left(\frac{z\lambda_{\text{vac}}}{\pi w_0^2}\right)^2}. \tag{2}$$

The fit (see Fig. 3E) suggests a minimum possible waist size of $w_0^{\text{metasurface}} = (0.56 \pm 0.03)$ um, even closer to the diffraction limit. Both results overlap within the experimental uncertainty. We attribute the deviation from the diffraction limit to imperfections in the EUV beam guiding and filtering optics, and possible residual corrugations of the silicon membrane. For comparison, achieving similar spot sizes using the near-infrared driving laser would require close to unity numerical apertures; in the EUV one only requires a numerical aperture of 0.05 (*36*).

Aside from the focusing power, the transmission properties are crucial for future applications. Photons with wavelengths shorter than 100 nm possess enough energy to overcome the band-gap of all known dielectrics, therefore large absorption is unavoidable (*37*). Nonetheless, owing to the vacuum guiding concept, our sample transmits more than 10% of all incoming 49 nm light and focuses 48% of the transmitted 49 nm light which limits the root mean squared metalens wavefront error (*38*) due to fabrication accuracy to $\lambda_{\text{vac}}/10$ ($\lambda_{\text{vac}} = 49$ nm, see (*19* Sec. 4) for details). Such fine-granular phase control is a prerequisite not only for focusing but opens the door for the future demonstration of optical angular momentum plates and general holograms at EUV wavelengths.

Simulation of Nyquist-limited focusing
To further explore the potential of EUV metalenses, we investigate a metalens design with focal length $f = 10$ um and overall optics diameter $d = 6$ um (see Fig. 4A for the phase profile and Fig. 4B for the final design). We then simulate the focusing of a linearly polarized Gaussian beam using finite difference time domain modeling (illuminating Gaussian beam waist $w^{\text{illum.}} = 2$ um, effective numerical aperture $\text{NA}_{\text{eff}} = \sin\left(\tan^{-1}\left(\frac{w^{\text{illum.}}}{f}\right)\right) \approx \frac{w^{\text{illum.}}}{f} = 0.2$ (*36*), corresponding to the maximum realizable numerical aperture given by the Nyquist sampling theorem and our unit cell size (*29*), see (*19* Sec. 1) for simulation details).

Fig. 4D shows the formation of the metasurface focus. Even under these challenging conditions, the metasurface focus closely approaches the diffraction limit ($w_0^{\text{diffraction limit}} = 85$ nm) with a minimum beam waist $w_0^{\text{metasurface}} = 94$ nm. The metalens focusing properties for a light pulse with extended bandwidth are explored in (*19* Sec. 5 and Fig. S6). Having the unit cell size be of the order of the design wavelength causes diffraction of approximately 53% of the incident power away from the beam axis into the diffraction orders of the quasi-periodic unit cell arrangement. Adding an unpatterned layer of silicon with refractive index $n = 0.77$ and a thickness on the order of half a wavelength after the metalens changes the grating condition in transmission and would prevent the creation of most of these propagating diffraction orders (as it limits the grating indices $p, q \in \mathbb{Z}$ which satisfy the transverse momentum wavevector condition $nk_0 =$

$\sqrt{\left(\frac{2\pi p}{\Delta x}\right)^2 + \left(\frac{2\pi q}{\Delta y}\right)^2 + (nk_z)^2}$ with the overall momentum k_0, and the momentum along the layer normal k_z).

For thorough comparison, we also model the focal profile of a binary absorption zone plate with equal numerical aperture (see Fig. 4A for the absorption profile and Fig. 4B for the design). The juxtaposition of the focal profiles generated by the zone plate and the metalens shown in Fig. 4D highlights striking differences in focus quality and corroborates the benefit of the novel metalens. Comparison to state-of-the-art technology (see (*39*) for a zone plate with comparable outermost zone width and (*19* Sec. 6) for a summary of EUV focusing optics) highlights that the zone plate creates side lobes in its focal plane, an unavoidable property of zone plate foci (*40*). In contrast, because the metasurface realizes the focusing phase profile accurately by suppressing spherical aberrations, no sidelobes are visible. Furthermore, as vacuum guiding decreases absorption and no energy is lost to sidelobes, the maximum intensity in the metasurface focus exceeds that of the zone plate by 9 %. The transverse focal cuts in Fig. 4C highlight this behavior: unwanted features present in the focal plane are suppressed by more than 10 dB for the metasurface compared to the zone plate.

<u>Concluding remarks</u>
The transfer of metasurface technology, with its associated superior design freedom to the EUV spectral region provides a general route to manufacture transmissive optics in this frequency range. This capability should lead to applications such as microscopy with unprecedented spatial and temporal resolution, orbital angular momentum beams with ultrahigh frequency, and structured light that has direct access to core level electronic transitions in atoms and molecules. EUV lithography has become the main enabling fabrication technology allowing us to keep up with Moore's law (*18*); on the other hand, metasurface based optics can be fabricated with deep UV lithography in the same semiconductor foundries of mainstream CMOS technology (*27*). This convergence of semiconductor processing technology and optics will expand to the realization of metaoptics using EUV lithography, further shrinking feature sizes and increasing the complexity of nanostructure shapes. In turn, with metasurfaces operating in the EUV, they will enable a new generation of lithography optics.

References and Notes

1. S. M. Kamali, E. Arbabi, A. Arbabi, A. Faraon, A review of dielectric optical metasurfaces for wavefront control. *Nanophotonics*. **7**, 1041–1068 (2018).

2. N. Yu, P. Genevet, M. A. Kats, F. Aieta, J.-P. Tetienne, F. Capasso, Z. Gaburro, Light propagation with phase discontinuities: generalized laws of reflection and refraction. *Science*. **334**, 333–337 (2011).

3. M. Khorasaninejad, W. T. Chen, R. C. Devlin, J. Oh, A. Y. Zhu, F. Capasso, Metalenses at visible wavelengths: Diffraction-limited focusing and subwavelength resolution imaging. *Science*. **352**, 1190–1194 (2016).

4. N. Mahmood, I. Kim, M. Q. Mehmood, H. Jeong, A. Akbar, D. Lee, M. Saleem, M. Zubair, M. S. Anwar, F. A. Tahir, J. Rho, Polarisation insensitive multifunctional metasurfaces based on all-dielectric nanowaveguides. *Nanoscale*. **10**, 18323–18330 (2018).

5. C. Spägele, M. Tamagnone, D. Kazakov, M. Ossiander, M. Piccardo, F. Capasso, Multifunctional wide-angle optics and lasing based on supercell metasurfaces. *Nat. Commun.* **12**, 3787 (2021).

6. R. C. Devlin, A. Ambrosio, N. A. Rubin, J. P. B. Mueller, F. Capasso, Arbitrary spin-to–orbital angular momentum conversion of light. *Science*. **358**, 896–901 (2017).

7. N. A. Rubin, G. D'Aversa, P. Chevalier, Z. Shi, W. T. Chen, F. Capasso, Matrix Fourier optics enables a compact full-Stokes polarization camera. *Science*. **365**, eaax1839 (2019).

8. Y. Intaravanne, X. Chen, Recent advances in optical metasurfaces for polarization detection and engineered polarization profiles: *Nanophotonics*. **9**, 1003–1014 (2020).

9. Y. Deng, X. Wang, Z. Gong, K. Dong, S. Lou, N. Pégard, K. B. Tom, F. Yang, Z. You, L. Waller, J. Yao, All-silicon broadband ultraviolet metasurfaces. *Adv. Mater.* **30**, 1802632 (2018).

10. K. Huang, J. Deng, H. S. Leong, S. L. K. Yap, R. B. Yang, J. Teng, H. Liu, Ultraviolet metasurfaces of ≈80% efficiency with antiferromagnetic resonances for optical vectorial anti-counterfeiting. *Laser Photonics Rev.* **13**, 1800289 (2019).

11. C. Zhang, S. Divitt, Q. Fan, W. Zhu, A. Agrawal, Y. Lu, T. Xu, H. J. Lezec, Low-loss metasurface optics down to the deep ultraviolet region. *Light Sci. Appl.* **9**, 55 (2020).

12. H. Liu, C. Guo, G. Vampa, J. L. Zhang, T. Sarmiento, M. Xiao, P. H. Bucksbaum, J. Vučković, S. Fan, D. A. Reis, Enhanced high-harmonic generation from an all-dielectric metasurface. *Nat. Phys.* **14**, 1006–1010 (2018).

13. A. Ahmadivand, M. Semmlinger, L. Dong, B. Gerislioglu, P. Nordlander, N. J. Halas, Toroidal dipole-enhanced third harmonic generation of deep ultraviolet light using plasmonic meta-atoms. *Nano Lett.* **19**, 605–611 (2019).

14. M. Semmlinger, M. Zhang, M. L. Tseng, T.-T. Huang, J. Yang, D. P. Tsai, P. Nordlander, N. J. Halas, Generating third harmonic vacuum ultraviolet light with a TiO2 metasurface. *Nano Lett.* **19**, 8972–8978 (2019).

15. M. L. Tseng, M. Semmlinger, M. Zhang, C. Arndt, T.-T. Huang, J. Yang, H. Y. Kuo, V.-C. Su, M. K. Chen, C. H. Chu, B. Cerjan, D. P. Tsai, P. Nordlander, N. J. Halas, Vacuum ultraviolet nonlinear metalens. *Sci. Adv.* **8**, eabn5644 (2022).

16. W. K. Tobiska, A. Nusinov, "Status of ISO draft international standard for determining solar irradiances (DIS 21348)" in *35th COSPAR Scientific Assembly* (Committee on Space Research (COSPAR), Paris, 2004), pp. 1–10.

17. F. Krausz, M. Ivanov, Attosecond physics. *Rev. Mod. Phys.* **81**, 163–234 (2009).

18. B. Turkot, S. Carson, A. Lio, "Continuing Moore's law with EUV lithography" in *2017 IEEE International Electron Devices Meeting (IEDM)* (IEEE, San Francisco, 2017), p. 14.4.1-14.4.3.

19. Materials and methods are available as supplementary materials at the Science website.

20. A. Thompson, D. Attwood, E. Gullikson, M. Howells, J. E. Kim, J. Kirz, J. Kortright, I. Linday, Y. Liu, P. Pianetta, A. Robinson, J. Scofield, J. Underwood, G. Williams, H. Winick, *X-ray data booklet* (Lawrence Berkeley National Laboratory, Berkeley, 2009).

21. D. L. Windt, IMD—Software for modeling the optical properties of multilayer films. *Comput. Phys.* **12**, 360–370 (1998).

22. E. D. Palik, G. Ghosh, Eds., *Handbook of optical constants of solids* (Academic Press, San Diego, 1998).

23. S. W. D. Lim, M. L. Meretska, F. Capasso, A high aspect ratio inverse-designed holey metalens. *Nano Lett.* **21**, 8642–8649 (2021).

24. M. Hentschel, K. Koshelev, F. Sterl, S. Both, J. Karst, L. Shamsafar, T. Weiss, Y. Kivshar, H. Giessen, Dielectric Mie voids: confining light in air. *Light Sci. Appl.* **12**, 3 (2023).

25. C. M. Smith, N. Venkataraman, M. T. Gallagher, D. Müller, J. A. West, N. F. Borrelli, D. C. Allan, K. W. Koch, Low-loss hollow-core silica/air photonic bandgap fibre. *Nature*. **424**, 657–659 (2003).

26. T. W. Ebbesen, H. J. Lezec, H. F. Ghaemi, T. Thio, P. A. Wolff, Extraordinary optical transmission through sub-wavelength hole arrays. *Nature*. **391**, 667–669 (1998).

27. J.-S. Park, S. Zhang, A. She, W. T. Chen, P. Lin, K. M. A. Yousef, J.-X. Cheng, F. Capasso, All-glass, large metalens at visible wavelength using deep-ultraviolet projection lithography. *Nano Lett.* **19**, 8673–8682 (2019).

28. W. T. Chen, A. Y. Zhu, V. Sanjeev, M. Khorasaninejad, Z. Shi, E. Lee, F. Capasso, A broadband achromatic metalens for focusing and imaging in the visible. *Nat. Nanotechnol.* **13**, 220–226 (2018).

29. S. M. Kamali, E. Arbabi, A. Arbabi, Y. Horie, A. Faraon, Highly tunable elastic dielectric metasurface lenses. *Laser Photonics Rev.* **10**, 1002–1008 (2016).

30. P. B. Corkum, Plasma perspective on strong field multiphoton ionization. *Phys. Rev. Lett.* **71**, 1994–1997 (1993).

31. M. Lewenstein, Ph. Balcou, M. Ivanov, A. L'Huillier, P. Corkum, Theory of high-harmonic generation by low-frequency laser fields. *Phys. Rev. A*. **49**, 2117–2132 (1994).

32. A. L'Huillier, K. J. Schafer, K. C. Kulander, Theoretical aspects of intense field harmonic generation. *J. Phys. B At. Mol. Opt. Phys.* **24**, 3315–3341 (1991).

33. A. H. Firester, M. E. Heller, P. Sheng, Knife-edge scanning measurements of subwavelength focused light beams. *Appl. Opt.* **16**, 1971–1974 (1977).

34. Robert L. Lucke, *Rayleigh-Sommerfeld diffraction vs Fresnel-Kirchhoff, Fourier propagation, and Poisson's spot* (Naval Research Laboratory, Washington, D.C., 2004).

35. B. E. A. Saleh, M. C. Teich, *Fundamentals of photonics* (Wiley, Hoboken, 2007).

36. H.-S. Chon, G. Park, S.-B. Lee, S. Yoon, J. Kim, J.-H. Lee, K. An, Dependence of transverse and longitudinal resolutions on incident Gaussian beam widths in the illumination part of optical scanning microscopy. *JOSA A*. **24**, 60–67 (2007).

37. M. Ossiander, K. Golyari, K. Scharl, L. Lehnert, F. Siegrist, J. P. Bürger, D. Zimin, J. A. Gessner, M. Weidman, I. Floss, V. Smejkal, S. Donsa, C. Lemell, F. Libisch, N. Karpowicz, J. Burgdörfer, F. Krausz, M. Schultze, The speed limit of optoelectronics. *Nat. Commun.* **13**, 1620 (2022).

38. M. Rimmer, Analysis of perturbed lens systems. *Appl. Opt.* **9**, 533–537 (1970).

39. J. Zhu, S. Zhang, S. Xie, C. Xu, L. Zhang, X. Tao, Y. Ren, Y. Wang, B. Deng, R. Tai, Y. Chen, Nanofabrication of 50 nm zone plates through e-beam lithography with local proximity effect correction for x-ray imaging. *Chin. Phys. B*. **29**, 047501 (2020).

40. G. W. Webb, I. V. Minin, O. V. Minin, Variable reference phase in diffractive antennas: review, applications, new results. *IEEE Antennas Propag. Mag.* **53**, 77–94 (2011).

41. V. Liu, S. Fan, S4 : A free electromagnetic solver for layered periodic structures. *Comput. Phys. Commun.* **183**, 2233–2244 (2012).

42. T. Takahagi, I. Nagai, A. Ishitani, H. Kuroda, Y. Nagasawa, The formation of hydrogen passivated silicon single-crystal surfaces using ultraviolet cleaning and HF etching. *J. Appl. Phys.* **64**, 3516–3521 (1988).

43. N. R. Böwering, A. I. Ershov, W. F. Marx, O. V. Khodykin, B. A. M. Hansson, E. Vargas L., J. A. Chavez, I. V. Fomenkov, D. W. Myers, D. C. Brandt, "EUV source collector" in *Proc. SPIE 6151, Emerging Lithographic Technologies X,* (SPIE, San Jose, 2006), p. 61513R.

44. B. Wu, A. Kumar, Extreme ultraviolet lithography: A review. *J. Vac. Sci. Technol. B Microelectron. Nanometer Struct.* **25**, 1743–1761 (2007).

45. C. Bourassin-Bouchet, M. M. Mang, F. Delmotte, P. Chavel, S. de Rossi, How to focus an attosecond pulse. *Opt. Express.* **21**, 2506–2520 (2013).

46. L. Poletto, F. Frassetto, F. Calegari, S. Anumula, A. Trabattoni, M. Nisoli, Micro-focusing of attosecond pulses by grazing-incidence toroidal mirrors. *Opt. Express.* **21**, 13040–13051 (2013).

47. H. Coudert-Alteirac, H. Dacasa, F. Campi, E. Kueny, B. Farkas, F. Brunner, S. Maclot, B. Manschwetus, H. Wikmark, J. Lahl, L. Rading, J. Peschel, B. Major, K. Varjú, G. Dovillaire, P. Zeitoun, P. Johnsson, A. L'Huillier, P. Rudawski, Micro-focusing of broadband high-order harmonic radiation by a double toroidal mirror. *Appl. Sci.* **7**, 1159 (2017).

48. P. P. Naulleau, K. A. Goldberg, P. J. Batson, S. Jeong, J. H. Underwood, Tolerancing of diffraction-limited Kirkpatrick–Baez synchrotron beamline optics for extreme-ultraviolet metrology. *Appl. Opt.* **40**, 3703–3709 (2001).

49. C. A. MacDonald, Focusing polycapillary optics and their applications. *X-Ray Opt. Instrum.* **2010**, 1–17 (2010).

50. E. Spiller, Reflective multilayer coatings for the far UV region. *Appl. Opt.* **15**, 2333–2338 (1976).

51. A. Guggenmos, U. Kleineberg, "Multilayer mirrors for attosecond pulses" in *Advances in Optics: Reviews, Vol. 1*, S. Y. Yurish, Ed. (International Frequency Sensor Association Publishing, Barcelona, 2018).

52. W. Chao, J. Kim, S. Rekawa, P. Fischer, E. H. Anderson, Demonstration of 12 nm resolution Fresnel zone plate lens based soft x-ray microscopy. *Opt. Express.* **17**, 17669–17677 (2009).

53. L. Drescher, O. Kornilov, T. Witting, G. Reitsma, N. Monserud, A. Rouzée, J. Mikosch, M. J. J. Vrakking, B. Schütte, Extreme-ultraviolet refractive optics. *Nature.* **564**, 91–94 (2018).

54. L. Quintard, V. Strelkov, J. Vabek, O. Hort, A. Dubrouil, D. Descamps, F. Burgy, C. Péjot, E. Mével, F. Catoire, E. Constant, Optics-less focusing of XUV high-order harmonics. *Sci. Adv.* **5**, eaau7175 (2019).

55. K. Keskinbora, U. T. Sanli, C. Grévent, G. Schütz, "Fabrication and x-ray testing of true kinoform lenses with high efficiencies" in *Proc. SPIE 9592, X-Ray Nanoimaging: Instruments and Methods II* (SPIE, San Diego, 2015), p. 95920H.

56. U. T. Sanli, H. Ceylan, I. Bykova, M. Weigand, M. Sitti, G. Schütz, K. Keskinbora, 3D nanoprinted plastic kinoform x-ray optics. *Adv. Mater.* **30**, 1802503 (2018).

57. E. Di Fabrizio, F. Romanato, M. Gentili, S. Cabrini, B. Kaulich, J. Susini, R. Barrett, High-efficiency multilevel zone plates for keV X-rays. *Nature*. **401**, 895–898 (1999).

58. L. Kipp, M. Skibowski, R. L. Johnson, R. Berndt, R. Adelung, S. Harm, R. Seemann, Sharper images by focusing soft X-rays with photon sieves. *Nature*. **414**, 184–188 (2001).

59. F. Salmassi, P. P. Naulleau, E. M. Gullikson, D. L. Olynick, J. A. Liddle, Extreme ultraviolet binary phase gratings: Fabrication and application to diffractive optics. *J. Vac. Sci. Technol. A*. **24**, 1136–1140 (2006).

60. P. P. Naulleau, F. Salmassi, E. M. Gullikson, E. H. Anderson, "Holographic optical elements for the extreme-ultraviolet regime" in *Proc. SPIE 6462, Micromachining Technology for Micro-Optics and Nano-Optics V and Microfabrication Process Technology XII* (SPIE, San Jose, 2007), p. 64620S.

61. F. Döring, B. Rösner, M. Langer, A. Kubec, A. Kleibert, J. Raabe, C. A. F. Vaz, M. Lebugle, C. David, Multifocus off-axis zone plates for x-ray free-electron laser experiments. *Optica*. **7**, 1007–1014 (2020).

Author Contributions:

M. O. developed the project, designed the metalenses, and conducted the numerical modeling. M. L. M. fabricated the samples. M. L. M., S. W. D. L., and M. O. imaged the samples. H. K. H., M. O., N.K., T.J., and M.S. designed, conducted, and analyzed the experiment. M. O., M. S., and F. C. wrote the manuscript. All authors discussed the final version of the manuscript.

Competing interests:

M. O., M. L. M., S. W. D. L., and F. C. have filed a provisional patent application (US 63/385,066). The authors declare no other competing interests.

Data and materials availability:

The data that support the findings of this study are included in the manuscript, the supplementary material, and in figshare with the identifier http://doi.org/10.6084/m9.figshare.22191457.

Supplementary Materials:

Materials and Methods

Figs. S1-S6

References (41-61)
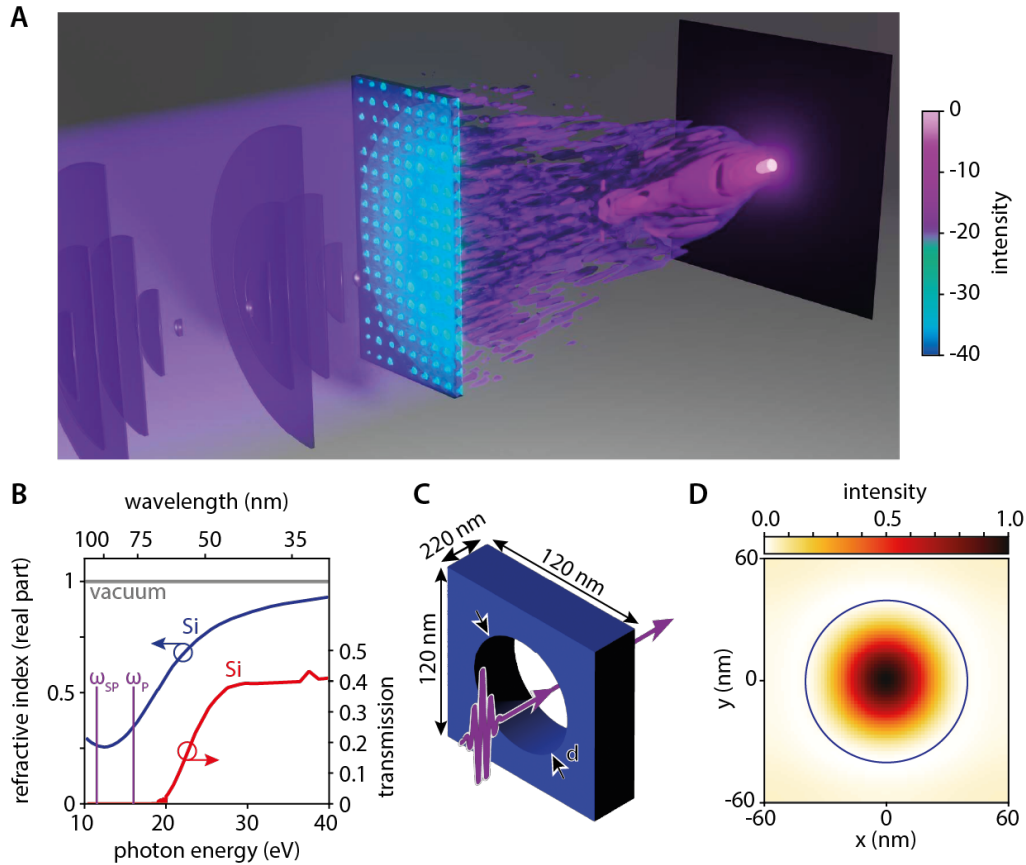
Fig. 1

Vacuum-guiding enables extreme ultraviolet metalenses.

(A) concept and simulation of a metalens focusing extreme ultraviolet light: we impart the phase profile of an aspheric focusing lens on light pulses with 50 nm vacuum wavelength (purple disks) using holes through a silicon membrane (rectangular area). Because the refractive index of silicon is smaller than unity in parts of the extreme ultraviolet spectrum, holes through silicon concentrate incoming light. This effect relaxes sub-wavelength requirements for creating metasurfaces, allows us to impart a hole-size-dependent phase shift using feature sizes on the order of the vacuum wavelength, and increases transmission through the absorbing membrane. The false color plot illustrates this light concentration in the holes and how the ultraviolet radiation collapses into a focus after propagating the focal length. For better visibility, we cut the displayed metasurface and the light intensity distribution along a plane that includes the optical axis. Further simulation details are presented in Fig. 4.

(B) photon energy-dependent real part of the refractive index of crystalline silicon (blue line, adapted from (*22*)) in the extreme ultraviolet spectrum and intensity transmission of a 220 nm thick silicon membrane (red line). The frequencies of the bulk ω_P and surface plasmon ω_SP are marked in purple.

(C) schematic and setup for metaatom simulation: extreme ultraviolet light (purple arrow) passes through a 220 nm thick crystalline silicon membrane (blue) with a hole with diameter d. We model a single unit cell (120 nm x 120 nm) with periodic boundary conditions.

(D) finite difference time domain (FDTD) simulation of extreme ultraviolet vacuum-guiding through an 80 nm diameter hole in a 220 nm thick silicon membrane. The false-color plot shows

13

the transverse beam intensity profile of light with 50 nm vacuum wavelength at the midpoint of the silicon membrane along the propagation direction, i.e., 110 nm after the front surface. The hole is indicated as a blue circle. Panel (C) shows the simulation setup in three dimensions. The hole covers 34 % of the total area, however, 84 % of the energy is transmitted within the hole and only 16 % of the energy is found in silicon. The intensity decays exponentially into the silicon cladding due to the refractive index contrast. The overall transmission of the patterned 220 nm thick silicon membrane is 67 %.
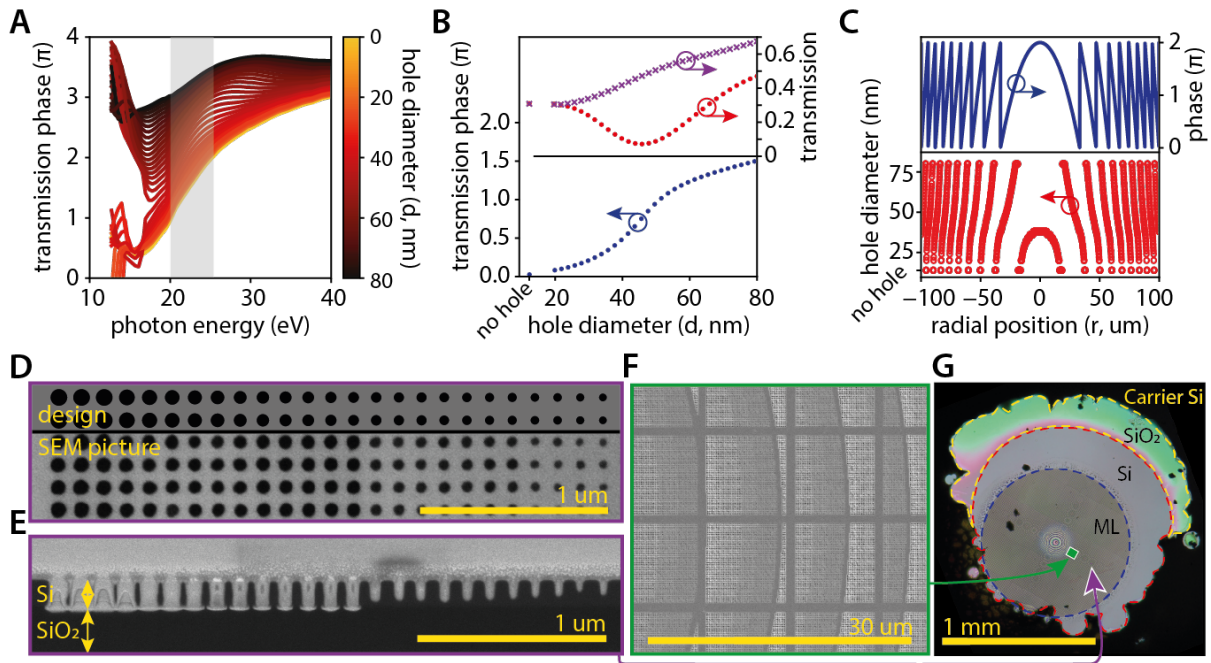
1

2 **Fig. 2**

3 **Design and fabrication of an extreme ultraviolet metalens.**

4 **(A)** photon energy-dependent transmission phase of holes in a 220 nm thick silicon membrane (see
5 Fig. 1C for the unit cell), color-coded for different hole sizes. The grey area indicates the region
6 where hole diameters from 20 nm to 80 nm offer phase coverage larger than $1.5\,\pi$, which is enough
7 to achieve efficient and diffraction-limited focusing (*27*).

8 **(B)** overall hole diameter-dependent intensity transmission (purple crosses) and transmission
9 phase in the forward direction (blue dots) of the resulting metaatom library at 50 nm wavelength
10 (25 eV photon energy). Because the 120 nm x 120 nm unit cell size is comparable to the
11 wavelength, low diffraction orders can be generated for holes that cause a transmission phase shift
12 close to π (diameters around 45 nm). When plotting only the transmission into the zeroth
13 diffraction order (red dots) of a periodic array of same-diameter holes, this causes a dip in the
14 transmission. Because hole diameters spatially vary in a metalens and light from all holes interferes
15 constructively to a focus, the more uniform overall transmission (purple crosses) is a better gauge
16 to judge transmission uniformity.

17 **(C)** target transmission phase profile (blue line) of a metalens with focal length $f = 10$ mm at 50
18 nm wavelength, calculated from equation (1) modulo 2π, and the corresponding matched hole
19 diameter (red circles) using the library of panel (B) to realize the metalens.

20 **(D)** lower panel: scanning electron microscope (SEM) picture of a 3 um x 0.5 um portion of the
21 metalens with 1 mm diameter and 10 mm focal length designed for 50 nm wavelength. The
22 position where the picture was taken on the metalens is marked by the purple arrow in panel (G).
23 The upper panel shows the design of the metalens in this area (compare with panel (C)).

24 **(E)** cross-section of a metalens fabricated using the same recipe as the lens in panel (D) on the
25 silicon-on-insulator carrier wafer obtained using focused ion beam milling and SEM. The position
26 where the picture was taken on the metalens is marked by the purple arrow in panel (G).

27 **(F)** zoomed-out SEM picture of a 34 um x 31 um portion of the metalens. The position where the
28 picture was taken on the metalens is marked by the green rectangle in panel (G). The focusing

15

pattern of the metalens is apparent as the ring segments with decreasing width from the left to right of the picture. Every 10 um, holes are omitted to increase the stability of the metalens, which is visible as a square scaffolding pattern. The symmetry of the scaffolding is intentionally different from the symmetry of the metasurface to increase stability.

(G) optical-microscope picture of the final metalens membrane. The metalens (ML) is encircled by the dashed blue line. Because its features are too small to be resolved at this magnification, the metalens shows a moiré pattern (ring patterns and bright area at the center, an enlarged image is provided in (*19* Fig. S4)). The unpatterned silicon membrane area appears solid grey (encircled by the dashed red line). Areas with remaining buried oxide layer appear red and green due to thin-film interference (encircled by the dashed yellow line). The silicon carrier wafer appears black.
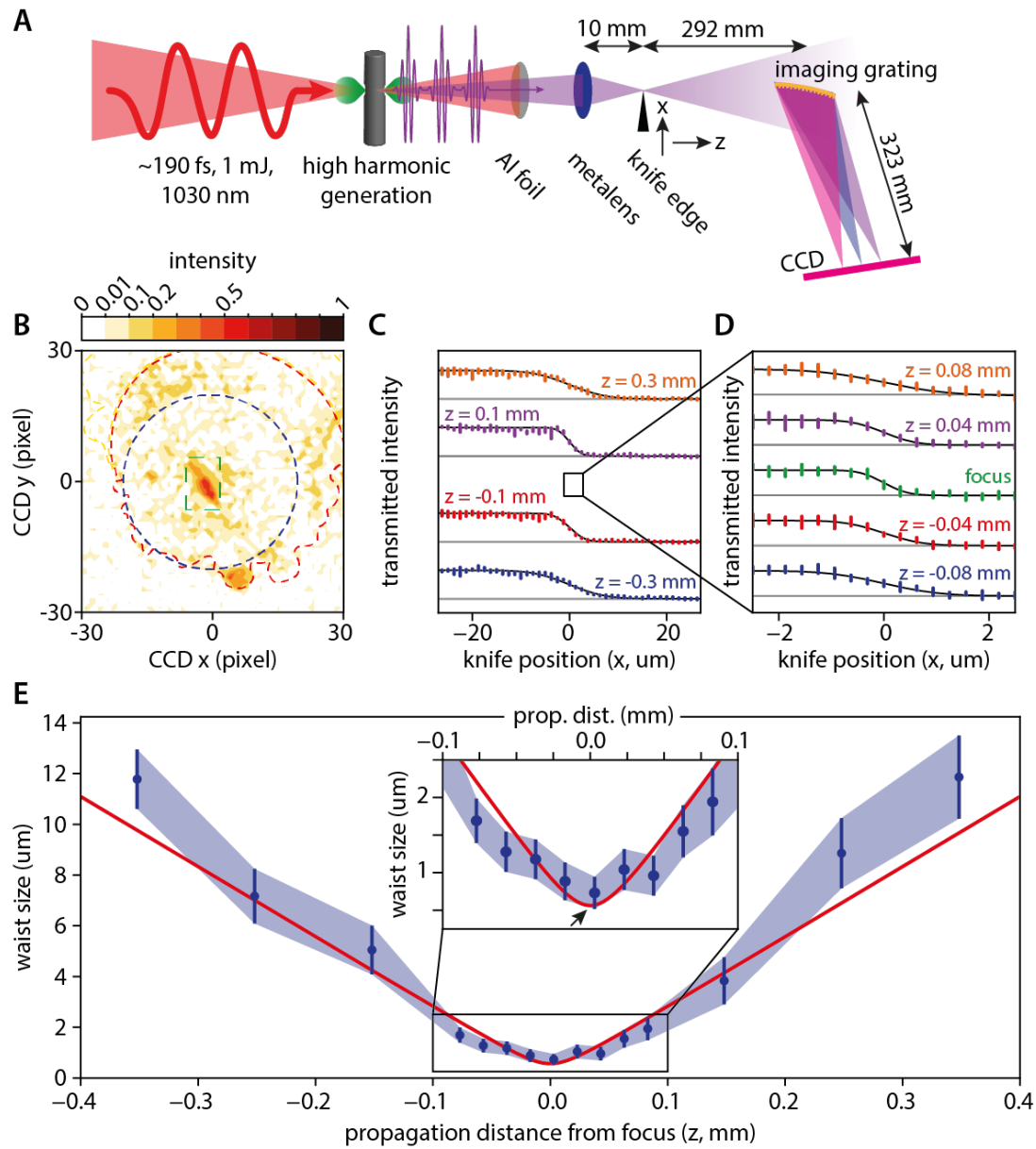
1
2 **Fig. 3**
3 **Experimental demonstration of extreme ultraviolet metalens focusing.**
4 **(A)** an intense near-infrared femtosecond laser pulse (red arrow and area) is focused into an argon
5 gas target (green) to generate an attosecond pulse train (purple arrow and area) via high harmonic
6 generation. Near-infrared radiation is blocked using an aluminum filter foil (grey). The attosecond
7 pulse train is then focused using the metalens (blue) pictured in Fig. 2. At the position of the focus
8 along the propagation direction (marked z), a knife-edge scan is performed using a razor blade
9 mounted on a piezo stage moving along the transverse beam direction (marked x). Afterward, the
10 attosecond pulse train's spectral components are split using a grazing incidence toroidal grating
11 and the focal plane is imaged on a charge-coupled-device (CCD) camera.
12 **(B)** extreme ultraviolet beam profile after the metasurface (false color plot) at 25.3 eV (21st
13 harmonic of the driving laser at 1030 nm wavelength) photon energy detected by the CCD. For

comparison, we repeat the outlines from the microscope picture in Fig. 2G: the dashed blue line marks the metasurface, and the dashed red line marks the unpatterned silicon area. The granular structure with low intensity is already present in the incoming beam profile, which is plotted in (*19* Fig. S5). The focal spot created by the metalens, imaged onto the CCD using the toroidal grating, is marked by the green dashed rectangle. It appears larger than the real focus due to the limited numerical aperture of the toroidal grating and aberrations caused by the imaging system.

(C) knife edge scans for different positions along the propagation direction of the metasurface-focused beam (movement direction marked z in panel (A)). The colored lines show the knife position-dependent (movement direction marked x in panel (A)) integrated photon flux detected by the CCD camera in the focus area. As the razor blade moves into the focus, it blocks part of the transmitted radiation and decreases the transmitted flux. A large negative derivative of the flux represents a small focus. The error bars represent the standard deviation of 3 measurements. The black lines are least-squares fits to the data assuming a Gaussian focus profile.

(D) same as panel (C) but in close proximity to the focus. The error bars represent the standard deviation of 10 measurements.

(E) propagation-direction dependent waist sizes extracted from the fits in panels (C) and (D) (blue dots). The error bars represent the 95% confidence interval. The red line is a fit to the waist sizes assuming Gaussian beam propagation. Inset: zoom-in-view of the propagation direction-dependent waist size close to the focus (extracted only from the fits in panel (D)). The minimum waist sizes reported in the text are marked by the black arrow.
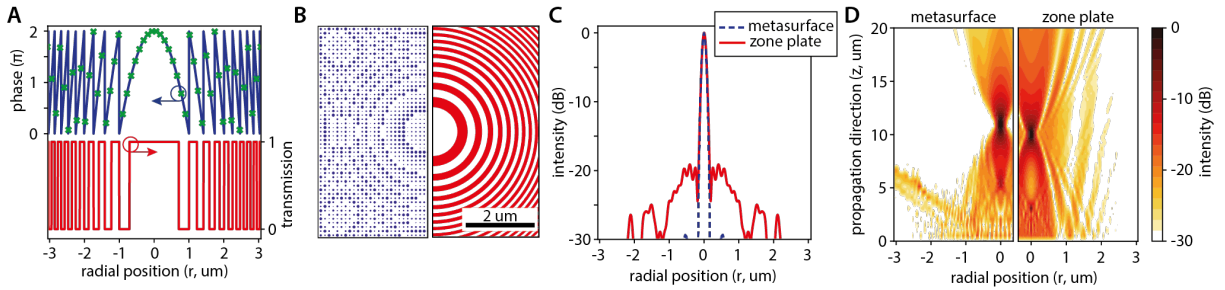
Fig. 4

Finite difference time domain modeling and benefits of an extreme ultraviolet metalens.

(A) target transverse phase profile (blue line) of a diffraction-limited metalens (focusing length $f = 10$ um, size 6 um x 6 um) designed for 50 nm wavelength (25 eV photon energy) and sampling of this phase profile with the library presented in Fig. 2 (green crosses). As a comparison, the transmission profile of a binary intensity Fresnel zone plate with the same numerical aperture, focal length, and size is also shown (red line).

(B) left panel: two-dimensional design of a metasurface realizing the phase profile in panel (A). White areas represent a 220 nm thick silicon membrane, and blue areas represent holes through the silicon membrane. Right panel: two-dimensional design of a binary intensity Fresnel zone plate realizing the transmission profile in panel (A). White areas are perfectly transmitting, and red areas are perfectly absorbing.

(C) modeled transverse intensity cuts through the focus generated by the metasurface (blue dashed line) and the zone plate in panel (B) (red line) for incoming light with 50 nm wavelength (25 eV photon energy) and illumination by a Gaussian beam with 2 um waist. The zone plate focus has characteristic side lobes which are not present in the metasurface focus.

(D) left panel: modeled light intensity evolution (false color plot) after the metasurface pictured in panel (B) focuses the Gaussian beam described in the caption of panel (C). right panel: modeled two-dimensional light intensity evolution (false color plot) after the zone plate pictured in panel (B) focuses the same Gaussian beam.

19

1
2
3
Supplementary Materials for
4
5
Extreme Ultraviolet Metalens by Vacuum Guiding
6
7
Marcus Ossiander[1, *, †], Maryna Leonidivna Meretska[1, †], Hana Kristin Hampel[2, †], Soon Wei
Daniel Lim[1], Nico Knefz[2], Thomas Jauk[2], Federico Capasso[1, *], Martin Schultze[2, *]
10
11
Correspondence to: mossiander@g.harvard.edu, capasso@seas.harvard.edu, schultze@tugraz.at
12
13
14
15
16 **This PDF file includes:**
17
18   Materials and Methods
19   Figs. S1 to S6
20   References (41-61)
21

Materials and Methods

1 Rigorous coupled wave analysis and finite-difference time-domain simulations

We use refractive index data for extreme ultraviolet radiation (EUV) distributed with the IMD software package (21). For this project, specifically, we used crystalline Silicon data reported by Edwards, Palik, and Ghosh (22). To obtain metaatom libraries, we calculate the hole-diameter dependent transmission phases for different square unit cell sizes using rigorous coupled-wave analysis (S4 (41)). To model full-device performance, we simulate a Gaussian beam incident on the perforated silicon membrane and a three-wavelength-thick vacuum spacer region before and after the membrane using finite-difference time-domain modeling (Ansys Lumerical FDTD). In this region, all near-fields decay, thus, we model the subsequent evolution using Rayleigh-Sommerfeld diffraction.

2 Fabrication

To allow fabrication of our metasurface, we require a minimum hole diameter of 20 nm and at least 40 nm distance between neighboring holes to retain membrane stability. To increase the stability of our membrane further, we omit holes in our design on a 1 um thick scaffolding grid spaced by 10 x 10 um (see Fig. 2F). The omission of holes does not limit the achievable focal spot but slightly decreases the efficiency (*27*). The fabrication of holes with accurate sub-100 nm diameter is challenging, therefore, we separate all holes into six groups using their diameter (20-30 nm, 30-40 nm, 40-50 nm, 50-60 nm, 60-70 nm, 70-80 nm) and use a different exposure dose and fabrication offset (i.e., the diameter we write during lithography is different than the diameter of the final etched hole) for each group.

The fabrication process is illustrated in Fig. S3: we start with a silicon-on-insulator wafer with a 220 nm thick silicon device layer, 3 um thick buried oxide layer, and 725 um thick silicon carrier layer. We deposit a silica hard mask layer using plasma-enhanced chemical vapor deposition (Surface Technology Systems). We then spin-coat a positive tone resist (MicroChemicals GmbH, AZ 4620) and expose marker structures using a maskless aligner (Heidelberg Instruments Mikrotechnik GmbH, MLA150). After development (MicroChemicals GmbH, AZ 400K) we etch the marker structures through the entire wafer (SPTS Technologies, Omega LPX Rapier) using reactive ion etching. In the following, we use the markers to align front and back side structures. We then spin-coat a layer of positive electron beam lithography resist (Zeon Corporation, ZEP520A). We then expose the metalens pattern using electron-beam lithography (Elionix, HS-50) and develop (o-Xylene). Subsequently, we transfer the metalens pattern first to the silica hard mask layer using inductively coupled plasma reactive ion etching (Surface Technology Systems, ICP RIE) and then to the silicon device layer using non-Bosch reactive ion etching (SPTS Technologies, Omega LPX Rapier). We then remove the silica hard mask layer using buffered Hydrofluoric acid. After defining the metalens pattern, we define the membrane area on the backside of the wafer using a spin-coated positive photoresist layer (MicroChemicals GmbH, AZ 4620) and a maskless aligner (Heidelberg Instruments Mikrotechnik GmbH, MLA150). After exposure and development (MicroChemicals GmbH, AZ 400K), we etch away the silicon carrier layer (SPTS Technologies, Omega LPX Rapier). To protect the thin membrane, we stop as soon as we can see the metasurface. This can leave behind a few microns of carrier silicon (less than 1 % of the initial thickness) at the bottom edges of the hole. We then remove the buried oxide layer by dripping hydrofluoric acid on the sample. Again, we stop the

process as soon as the metasurface is uncovered. The non-uniform black pattern in Fig. S4 is remaining silicon at the bottom edges of the hole with the bubble-shaped edges caused by the wet etch. As long as the entire metasurface is uncovered, we do not further remove it. The hydrofluoric acid wet etch also minimizes the formation of a silicon native oxide which strongly absorbs EUV (*42*).

The presented concept and simulations can be transferred directly to shorter wavelengths. However, as other materials must be used (e.g., for 13.5 nm wavelength, palladium, rhenium, or ruthenium), the fabrication recipe must be adapted. The electron beam lithography step is challenging for the feature pitches and sizes required at 13.5 nm wavelength but within the manufacturer specifications of available tools. As shorter wavelengths require less material thickness for a 2π phase shift, the required holes' aspect ratios are similar and thus the etch process remains achievable. If the membrane thickness gets too thin to support itself, an unpatterned support can be added (e.g., a thin silicon membrane at 13.5 nm wavelength).

3 Laser System, high-harmonic-generation, and measurement setup.

We start with femtosecond pulses (1 mJ energy, 6 kHz repetition rate, 161 fs full-width-at-half-maximum pulse duration, 1030 nm wavelength) from an ytterbium-based and diode-pumped laser (Light Conversion, UAB, Pharos). In a high-vacuum environment, we focus these laser pulses (f = 25 cm) into an invar tube filled with argon gas to create an EUV attosecond pulse train via HHG. We adjust the argon pressure to achieve phase matching between the fundamental driving pulses and radiation generated at 25 eV photon energy (approx. 10 mbar argon pressure). The final HHG radiation contains spectral components from the fundamental photon energy to above 40 eV. We then route the generated radiation to the metasurface using an uncoated gold mirror (Thorlabs, Inc.) and filter spectral components below 20 eV photon energy using a 0.5 um thick aluminum foil (Lebow Co.). After the metasurface, we perform a knife-edge scan using a razor blade mounted on a piezo nanopositioner (Piezosystem Jena GmbH). We then disperse the transmitted radiation spectrally using a toroidal grating (450 lines per mm, 153 mm focal length, 8 mm usable aperture, Horiba, Ltd., 541 00 200) and detect radiation using a back-thinned charge-coupled-device camera (Greateyes GmbH, GE 1024 256 BI UV1) protected by an additional 0.5 um thick aluminum foil.

4 Efficiency determination

To evaluate the efficiency of the EUV metalens, we compare the incoming photon flux in the region of the metasurface Φ^{incoming} (area marked by the blue dashed circle in Fig. S5), the entire photon flux transmitted through the sample $\Phi^{\text{transmitted}}$, and the photon flux change $\Delta\Phi^{\text{knife edge}}$ recorded in the knife edge scan with the knife retracted and blocking the focus (see Fig. S5C). To determine the fraction of light not influenced by the metasurface we subtract the detected focused light $\Delta\Phi^{\text{knife edge}}$ from the entire photon flux transmitted through the sample $\Phi^{\text{transmitted}}$. Because the inserted razorblade only covers 0.6% more of the metasurface area than the retracted razorblade, we neglect its influence on the detected background field. Light lost to grating effects is diffracted to large angles and is never detected and not included in the overall transmission, the background field, or the focused intensity.

Furthermore, because the numerical aperture of the imaging grating is smaller than that of our metasurface, some light that is focused by the metalens is not detected. To estimate the collection efficiency, we use the measured beam profile (Fig. S5) and project it into the grating plane along the propagation direction using the focal distance of the metalens, the distance between

the metalens and the grating, and the effective free aperture of the grazing incidence imaging grating. We find that $\approx 14\%$ of the focused radiation is collected by the imaging grating and correct $\Delta\Phi^{\text{knife edge}}$ to obtain Φ^{focused}. We find the ratios

$$\frac{\Phi^{\text{transmitted}}}{\Phi^{\text{incoming}}} = 11\%, \frac{\Phi^{\text{focused}}}{\Phi^{\text{transmitted}}} = 48\%, \text{ and } \frac{\Phi^{\text{focused}}}{\Phi^{\text{incoming}}} = 5.5\%.$$

The theoretically predicted average metaatom transmission (see purple crosses in Fig. 2B) is 40 %. As discussed in the main manuscript (see Simulation of Nyquist-limited focusing), with the current unit cell configuration, we expect to lose about 53 % of the transmitted power to low-order diffraction, yielding $\left(\frac{\Phi^{\text{transmitted}}}{\Phi^{\text{incoming}}}\right)^{\text{theory}} = 19\ \%$. If we furthermore include 25% absorption in a 2 nm thick native silicon oxide, we expect $\left(\frac{\Phi^{\text{transmitted}}}{\Phi^{\text{incoming}}}\right)^{\text{theory,2 nm oxide}} = 14\ \%$, comparable to the observed $\frac{\Phi^{\text{transmitted}}}{\Phi^{\text{incoming}}} = 11\ \%$.

To estimate the wavefront accuracy of the metalens from the focusing efficiency, we solve the Rayleigh Sommerfeld diffraction integral (34) for an incoming Gaussian beam focused by the phase profile of a diffraction-limited lens. This phase profile is modified by wavefront errors caused by a) the areas where holes are omitted to mechanically stabilize the metasurface (compare with Fig. 2F), b) the phase coverage being limited to 1.5 π, and c) fabrication accuracy. 48 % focusing efficiency is caused by a root mean squared (RMS) wavefront error of $\lambda_{\text{vac}}/7.3$ ($\lambda_{\text{vac}} = 49.0$ nm). The omitted-hole areas alone cause an RMS wavefront error of $\lambda_{\text{vac}}/11.0$. The limited phase coverage alone causes an RMS wavefront error of $\lambda_{\text{vac}}/27.9$. Together, both yield an RMS wavefront error of $\lambda_{\text{vac}}/10.3$. Therefore, to explain the recorded focusing efficiency, we calculate an RMS wavefront error due to fabrication accuracy of $\lambda_{\text{vac}}/10.0$.

5 Focusing over an extended bandwidth.

The metalens also focuses light away from the design wavelength. Solving equation (1) for f yields:

$$f = \frac{\lambda_{\text{vac}}\,\varphi}{4\pi} - \frac{r^2\pi}{\varphi\lambda_{\text{vac}}} \approx -\frac{r^2\pi}{\varphi\lambda_{\text{vac}}}.$$

For numerical apertures smaller than 0.2, the second term dominates, and we can approximate the hyperbolic phase profile with a quadratic phase profile with less than 1% error. The exact phase φ imparted by a hole changes with the wavelength. However, the positions within a metalens at which holes with the same diameters occur (i.e., the radial zones in which the phase increases from 0 to 2π) remain the same. Therefore, for off-design wavelengths λ_{vac}, the focal length $f(\lambda_{\text{vac}})$ will shift compared to the design wavelength $\lambda_{\text{vac}}^{\text{design}}$ and design focal length f^{design} according to:

$$f(\lambda_{\text{vac}}) \approx f^{\text{design}}\frac{\lambda_{\text{vac}}^{\text{design}}}{\lambda_{\text{vac}}}.$$

High bandwidth is often required by applications with time resolution. As a test, we choose 2 eV bandwidth (supporting pulse durations down to 0.9 fs). Fig. S6 presents the focus of the metalens examined in Fig. 4 of the manuscript for light with 24, 25, and 26 eV photon energy. We

4

observe a clean focus over the entire bandwidth, with a focal shift less than the Rayleigh range, suggesting metalenses are applicable to ultrashort light pulses.

However, for photon energies far away from the design energy, the phase coverage within a zone will start deviating significantly from 2π. A simulation for 30 eV photon energy in Fig. S6D shows the effects: the focusing efficiency drops, sidelobes around the focus appear, and grating effects worsen.

6 Optics for EUV and soft x-rays

Due to the strong absorption of all materials, most state-of-the-art EUV optics, e.g., spherical and toroidal mirrors, Kirkpatrick-Baez doublets, and polycapillary optics (43–49) rely on reflection. Acceptable reflectivities are often only achievable for light with grazing incidence, which demands bulky optics. Together with requirements for high-quality surfaces, low wavefront errors, and specialized metallic and multilayer coatings (50, 51), this limits achievable numerical apertures and aggravates cost. As transmissive optics, absorptive Fresnel zone plates (52) have been demonstrated. The lack of usable optics also led to the exploration and demonstration of EUV focusing via gas plumes of resonant atoms (53) and preconditioning driving radiation and subsequent nonlinear frequency upconversion (54). In the soft x-ray spectrum (photon wavelength range 0.1 nm - 10 nm, photon energy range 124 eV - 12 keV (16)), material limitations - especially absorption - are partially relieved, and focusing can be achieved using refractive kinoform lenses (55, 56), few-step phase zone plated (57) and photon sieves (58). Furthermore, reflective binary phase control was demonstrated but with many-wavelength large feature sizes (59–61).

1
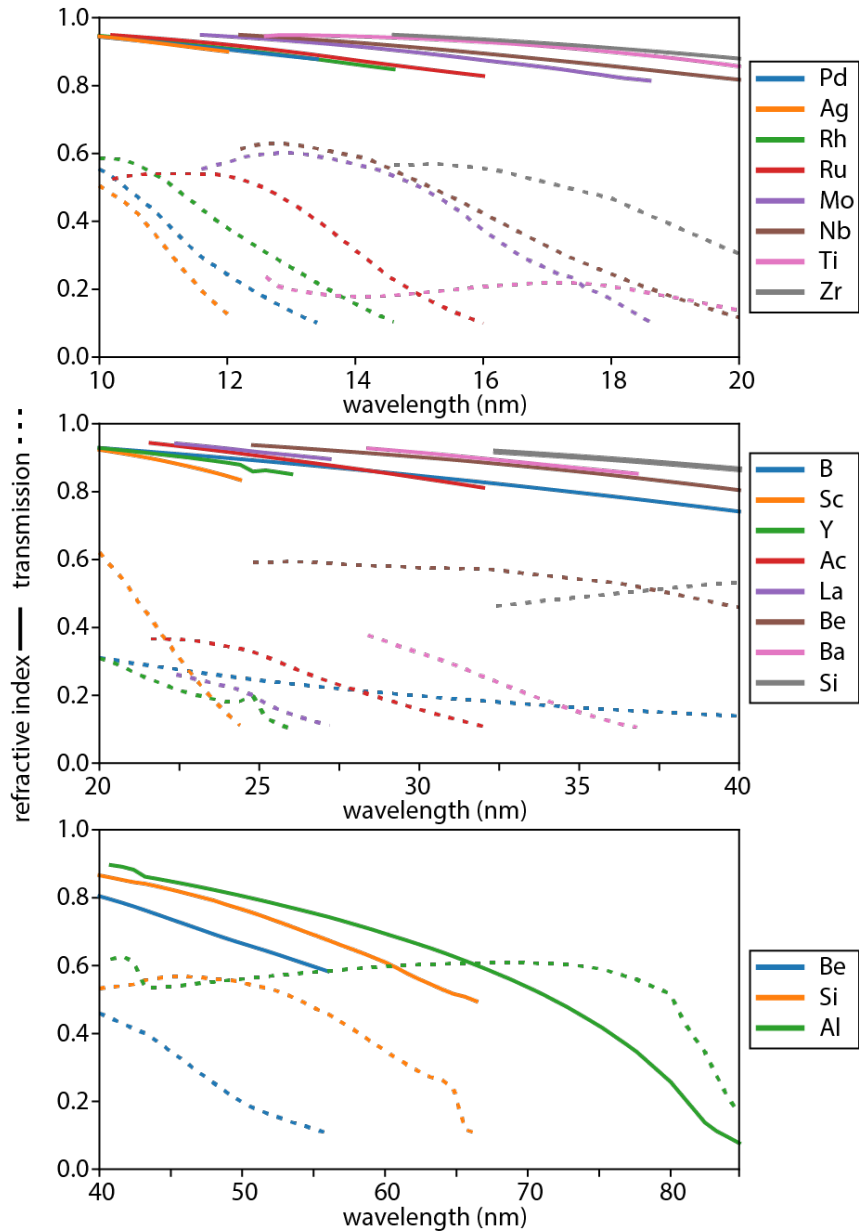
Fig. S1. Refractive indices of different materials in the EUV.
The wavelength-dependent real part of the refractive index is plotted as solid lines. Realizing a metasurface requires tuning the transmission phase within its limited thickness. The effective refractive index of a waveguide usually lies between the refractive index of the core (in this case vacuum, $n = 1$) and the cladding ($n < 1$). Therefore, the transmission of a solid layer of material with a thickness that induces a 2π propagation phase shift compared to propagation through the same thickness of vacuum yields a lower limit for the transmission of realizable metaatoms. We plot the transmission of layers of the respective materials at this 2π propagation phase thickness as dotted lines. Data is only displayed in spectral regions where the transmission at this 2π propagation phase thickness is larger than 10%. Data was taken from (*21*).

1
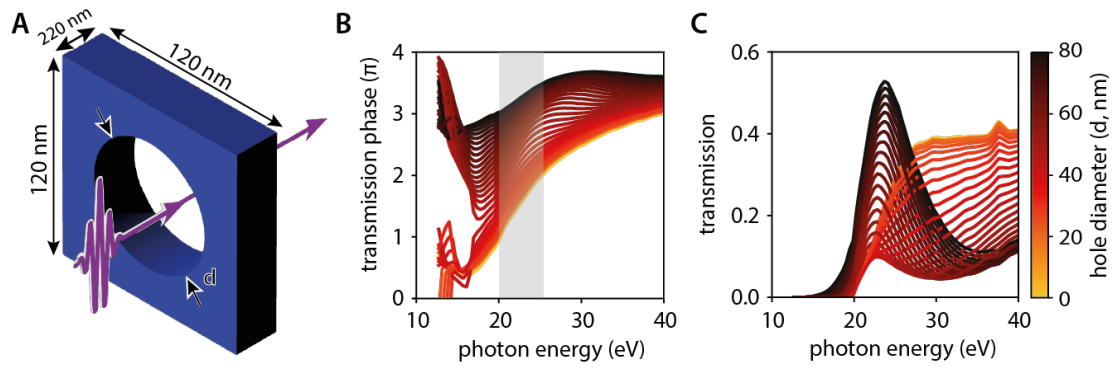
Fig. S2. Energy-dependent extreme ultraviolet transmission through a perforated membrane in the forward direction.

(A) simulation setup: we model the transmission of extreme ultraviolet light (purple arrow) passing through a 220 nm thick crystalline silicon membrane (blue) with a hole with diameter d. We model a single 120 nm x 120 nm unit cell with periodic boundary conditions.

(B) photon energy and hole diameter-dependent transmission phase (colored lines, see the color bar in panel (C)) of the 220 nm thick Silicon membrane with a hole. The grey area indicates the region where hole diameters from 20 nm to 80 nm offer phase coverage larger than 1.5 π.

(C) photon energy and hole diameter-dependent intensity transmission into the zeroth diffraction order (colored lines) of the 220 nm thick silicon membrane with a hole.
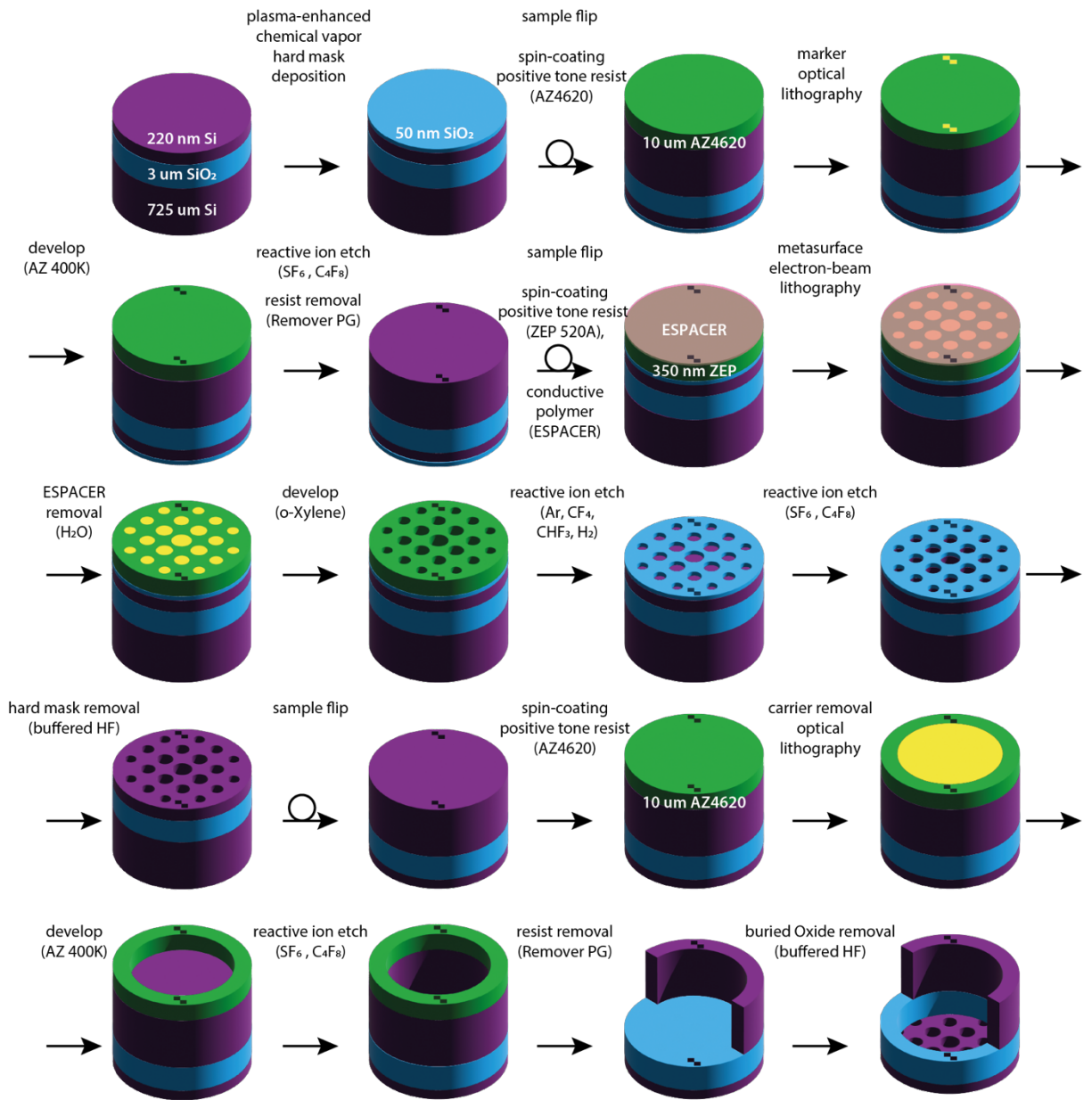
Fig. S3. Extreme ultraviolet metasurface fabrication (not to scale)

The base material is a silicon-on-insulator (SOI) wafer, consisting of a 220 nm device layer (silicon, purple), a 3 um buried oxide layer (silica, blue), and a 725 um carrier wafer (silicon, purple). A silica hard mask (blue) is deposited via chemical vapor deposition. The sample is spin-coated with a positive tone resist (green) and marker structures (yellow) are exposed using optical lithography. The exposed resist is removed using developer, and the entire wafer is etched away in these areas using reactive ion etching to create markers for aligning front and back side structures. Remaining resist is removed. Then, a positive tone electron beam lithography resist (green) and a conductive polymer (pink) are spin-coated. The metasurface pattern is written (yellow) using electron beam lithography, then the conductive polymer and the exposed resist are

1   removed using water and developer. The pattern is first etched through the hard mask and then
2   through the device layer using reactive ion etching. The hard mask is removed using buffered
3   Hydrofluoric acid. To create a free-standing membrane, positive tone resist is spin-coated on the
4   back side of the sample (green), and the metasurface area is exposed using optical lithography
5   (yellow). The exposed resist is removed using developer, and the Silicon carrier wafer is etched
6   away in this area using reactive ion etching. Finally, the remaining resist is removed, and the buried
7   oxide layer is etched away in the same area using buffered hydrofluoric acid.
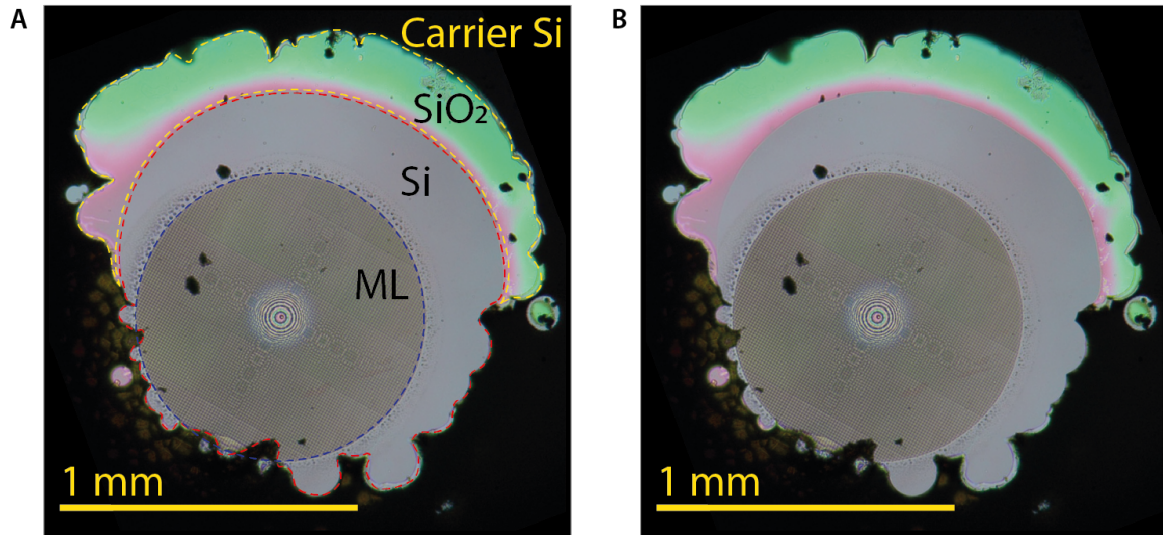
Fig. S4. Optical-microscope pictures of the final metalens membrane.

(A) With the overlay reproduced from Fig. 2G and Fig. 3B: the metasurface lens (ML) is encircled by the dashed blue line. Because the metalens features are too small to be resolved at this magnification, it shows a moiré pattern (ring patterns and bright area at the center). The unpatterned silicon membrane area appears solid grey (encircled by the dashed red line). Areas with remaining buried oxide layer appear red and green due to thin-film interference (encircled by the dashed yellow line). The silicon carrier wafer appears black.

(B) The same picture without the overlay.
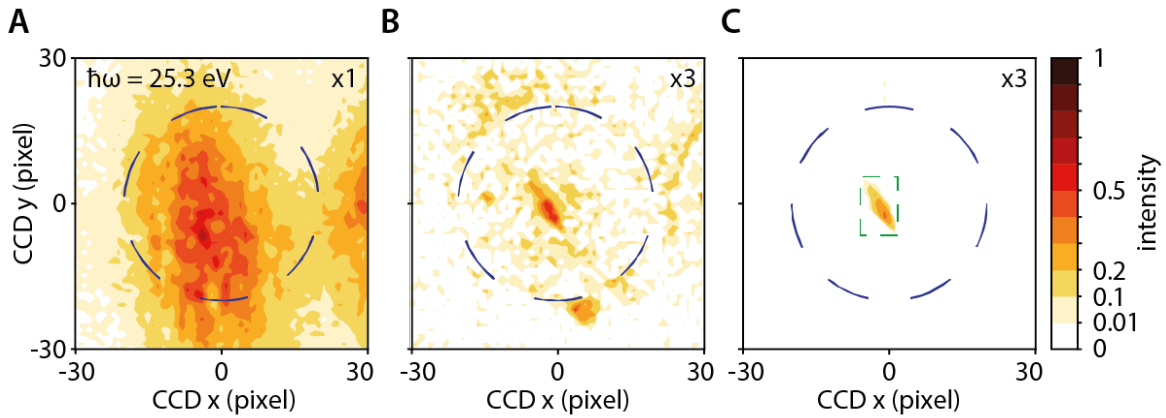
Fig. S5. Real space images of the experimental metalens focal plane.

(A) incoming extreme ultraviolet beam profile (false color plot) at 25.3 eV photon energy (21st harmonic of the driving laser at 1030 nm wavelength) detected by the CCD. The dashed blue line marks the circumference of the metasurface (not inserted into the beam in this panel). Color bar in panel (C).

(B) extreme ultraviolet beam profile after the metasurface (false color plot) at 25.3 eV photon energy detected by the CCD. The dashed blue line marks the circumference of the metasurface. Color bar in panel (C), the photon flux was multiplied by a factor of 3 when compared with panel (A). This does not mean the focused intensity is smaller than the incoming beam intensity: because the imaging grating has a smaller numerical aperture than the metalens, only 14 % of the focused light is collected. Furthermore, aberrations caused by using a grazing incidence toroidal imaging grating enlarge the observed focus compared to the real focus. The focal spot size measured using the knife-edge scan is considerably smaller than a single pixel of our CCD camera and yields an intensity enhancement in the focus of more than 27000.

(C) extreme ultraviolet fraction detected by the CCD that was focused by the metasurface (false color plot). We isolate focused radiation by subtracting a picture taken with the razor blade obstructing the focus from a picture without the razor blade blocking the focus. The dashed blue line marks the circumference of the metasurface. The dashed green line marks the light focused by the metalens. The photon flux was multiplied by a factor of 3 when compared with panel (A).

11
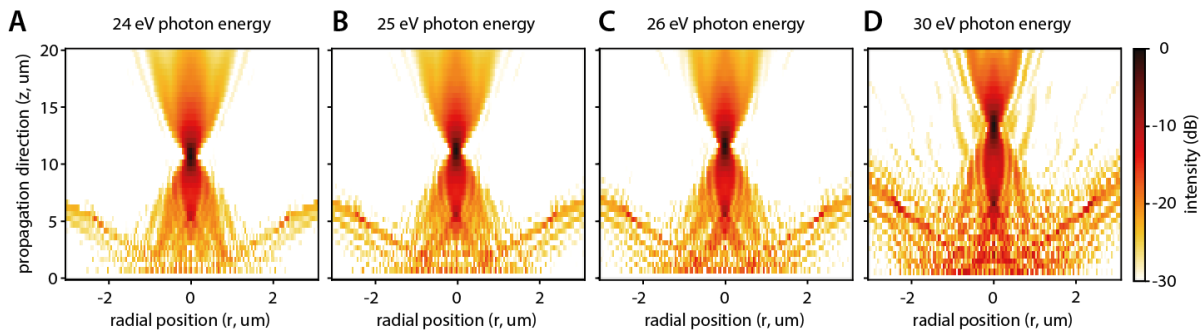
Fig. S6. Focusing over an extended bandwidth.

(A) modeled light intensity evolution (false color plot) after the metasurface pictured in Fig. 4B focuses light with 24 eV photon energy. Color bar in panel (D).

(B) same as (A) for 25 eV photon energy.

(C) same as (A) for 26 eV photon energy.

(D) same as (A) for 30 eV photon energy.